Nonlinear Dyn (2022) 109:609–629
https://doi.org/10.1007/s11071-022-07501-8

ORIGINAL PAPER

Study on the bistable vibration behaviour of a rod-fastened rotor-bearing system

Jiaqi Li · Zhongyu Yang · Qingzhao Ren · Guyun Mo · Wenyuan Zhong · Yinli Feng · Guoqing Li

Received: 8 November 2021 / Accepted: 29 April 2022 / Published online: 7 May 2022
© The Author(s), under exclusive licence to Springer Nature B.V. 2022

Abstract Gas turbine generator sets are widely used in IGCC system, gas-steam combine cycle, distributed energy system et al. for its advantages of low pollution, high efficiency, quick start and stop. The structure of gas turbine rotor can be divided into integral rotor and rod-fastened rotor. Experimental study shows that the vibration signal, especially the displacement signal, of the rod-fastened rotor will increase/decrease greatly in a small interval of rotating speed. The reason for this phenomenon is the unique structure of the rod-fastened rotor, namely the interfaces between discs. In this paper, based on the Lagrange equation, the equation of motion of a rod-fastened rotor-bearing system considering the damping of the contact interface is established. The bistable behaviour and hysteretic cycle, also called the jumping phenomenon in engineering, are revealed. In addition, a test bench of the rod-fastened rotor-bearing system is built. The bistable behaviour and hysteretic cycle are experimentally proven, and the effect of the eccentric distance of the rotor on the bistable behaviour is experimentally explored.

Keywords Rod-fastened rotor-bearing system · Damping of interface · Nonlinear oil film · Bistable behaviour · Hysteretic cycle

J. Li (✉) · Z. Yang · Q. Ren · G. Mo · W. Zhong · Y. Feng · G. Li
Key Laboratory of Light Duty Gas Turbine, Institute of Engineering Thermophysics, Chinese Academy of Sciences, Beijing 100190, China
e-mail: lijiaqi@iet.cn

J. Li · Z. Yang · G. Mo · W. Zhong · Y. Feng · G. Li
School of Engineering Sciences, University of Chinese Academy of Sciences, Beijing 100049, China

J. Li · Z. Yang · Q. Ren · G. Mo · W. Zhong · Y. Feng · G. Li
Innovation Academy for Light-Duty Gas Turbine, Chinese Academy of Science, Beijing 100190, China

1 Introduction

A rotor-bearing system is the core component of a rotating machine, and its dynamic behaviour affects the efficiency, vibration, and stability of the system [1]. Studies on the dynamic behaviour of integral rotor-bearing systems are listed in the literature [2–6]. Rod-fastened rotors are widely used in light-duty aero engines and heavy-duty gas turbines due to their high strength, light weight, and easy assembly and disassembly. Unlike the integral rotor, the rod-fastened rotor is not a whole in the structure, and all discs are tied together by rods [7]. A typical rod-fastened rotor-bearing system is shown in Fig. 1. However, due to the discontinuity of the rotor, the dynamic behaviour would become more complicated.

The bistable behaviour of rod-fastened rotor is a phenomenon of the difference of dynamic behaviour during acceleration and deceleration. It can be known

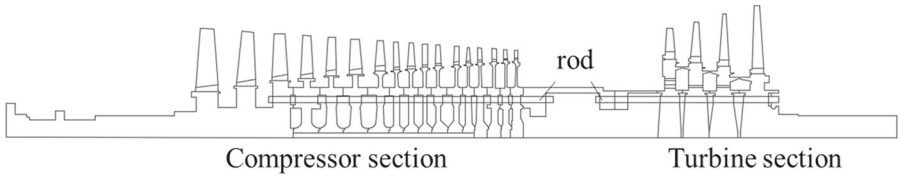

Fig. 1 A typical rod-fastened rotor structure [8]

from Li [9], the main reasons for the bistable behaviour include nonlinear oil film force, nonlinear stiffness, damping of the interface, etc.

In terms of the nonlinear oil film, Hei et al. modelled a rod-fastened rotor-hydrodynamic journal-bearing system [10], rod-fastened rotor-fixed-tilting pad journal-bearing system [11] and rod-fastened rotor-finite length-bearing system [12], and the numerical method was applied to reveal the nonlinear dynamic behaviours of these systems. These studies presented period-1, period-2, period-4, quasiperiodic motion, etc. nonlinear behaviours. Li et al. [13] deduced the equation of motion of a rod-fastened rotor-ball-bearing system considering bearing clearance, gyroscopic moment, initial deformation, and other factors. The Runge–Kutta–Fehlberg method was used to explore the nonlinear dynamic behaviour of the system. This research held that a larger bearing clearance and initial deflection might decrease the speed at which the system enters chaotic motion. Sun et al. [14] studied the effect of the temperature of the lubricating oil film on the pressure distribution and also the influence of the temperature of the lubricating oil film on the dynamic characteristics of rotor-bearing systems. Haslam et al. [15] proposed a novel method combining the Jeffcott rotor-detailed bearing model with the generalized harmonic balance method. The effect of radial oil clearance of bearing on the unbalance response and stability of system was studied. Alves et al. [16] experimentally explored the effect of the oil film nonlinearity in bearings on the rotor balancing. Zhao et al. [17] proposed a dynamic model of hydrodynamic journal bearings under large perturbations.

From the perspective of the nonlinear stiffness and damping of the interface, Zhuo et al. [18] proposed the equivalent model of the bending stiffness of the contact interface of a rod-fastened rotor, which laid a foundation for subsequent studies. Qian et al. [19] established a finite element model of an aero-engine rotor considering the nonlinear stiffness of the contact interface, and the hard stiffness characteristic was revealed by the harmonic balance method. Zhang et al. [20] set up a dynamic model of a rod-fastened rotor considering the time-varying stiffness of the interface. The unbalanced response was calculated by the harmonic balance method. This research argued that the rod-fastened rotor presents soft stiffness characteristics considering the stiffness time-varying characteristics. Cheng et al. [21] calculated the vibration response of rod-fastened rotors by the harmonic balance method combined with the prediction-correction and homotopy algorithms. The effect of nonlinear stiffness, eccentricity and eccentric phase angle on the bistable vibration characteristics was studied. However, this pioneering work did not involve the study of the damping of the interface. Wang et al. [22, 23] devised a dynamic model of the rod-fastened rotor considering the nonlinear restoring force at the contact interface, the internal damping of the disc and the nonlinear oil film force. The theoretical analysis of the bistable vibration behaviour was explored. However, this work did not involve the damping of the interface and experimental research. Li et al. [24] presented the experimental and numerical studies on the stiffness and damping properties of rod-fastened rotor with interference fits under different preloads.

Besides, in some cases, the machining error of rotor [25–31], rub-impact force and other nonlinear coupling forces [32–40] would also lead to bistable behaviour of rotor.

Despite recent developments in nonlinear excitation and the response of rod-fastened rotors, the nonlinear behaviour of damping of interfaces is rarely considered, and the bistable test is even less involved. Thus, the main objective of this paper is to reveal the effect of damping of the interface on the nonlinear behaviour of the system. As a basic step, the equation of motion of the system considering the damping of the interface is set up based on the Lagrange equation. On this basis, the fourth-order Runge Kutta method is employed to analyse the dynamic behaviour of the

system, and the bistable behaviour and hysteretic cycle are revealed. Moreover, a test bench of rod-fastened rotor-bearing system was built, which is a step further from the previous work. The bistable behaviour and hysteretic cycle were experimentally indicated, and the influence of the eccentric distance of the rotor on the bistable behaviour was experimentally studied. The research in this paper can provide theoretical guidance for bistable behaviour and hysteresis cycle in rod rotor test, and the experimental results can provide a basis for reducing the bistable vibration.

2 Model of the rod-fastened rotor-bearing system with damping of the interface

The inherent structural features of a rod-fastened rotor include fastening rods and interfaces between discs. Due to the discontinuity of the rotor, the interface would produce additional damping, further complicating the dynamic behaviour of the system. In this paper, a dynamic model of the rod-fastened rotor considering interface damping is set up (depicted in Fig. 2), and the nonlinear behaviour is explored via a numerical method.

The rod-fastened rotor-bearing system is highly complex, and the assumptions below are proposed to simplify the system.

1. The bearings on both sides are identical.
2. The phase angle of mass eccentricity at each disc is the same.
3. There is no separation of discs during the operation.

The sketch of simplified system is shown in Fig. 3.

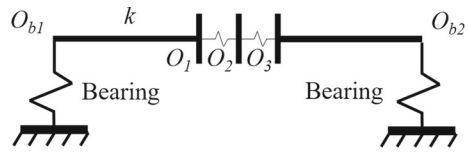

Fig. 3 The sketch of simplified system

The equation of motion of rod-fastened rotor-bearing system will be deduced in this section, the flowchart of deriving is shown in Fig. 4.

2.1 Equation of motion

m_i (i = 1–5) is the lumped mass of the rotor, k_{shaft} is the stiffness of the shaft, k_{in} is the bending stiffness of the interface, c_1 is the damping coefficient of the bearing, c_2 is the damping coefficient of the disc, and c_3 is the damping coefficient of the interface. The equation of motion can be deduced by the Lagrange equation.

The Lagrange equation can be expressed as:

$$\frac{d}{dt}\left(\frac{\partial L}{\partial \dot{q}_i}\right) - \frac{\partial L}{\partial \dot{q}_i} + \frac{\partial D}{\partial \dot{q}i} = f_i(i = 1, 2, ..., n), \tag{1}$$

where L is the Lagrange function, and $L = V - U$. V is the kinetic energy of the system, U is the potential energy of the system, D is the dissipation energy of the system, q_i and $\dot{q}_i$ are generalized coordinates and velocities of the system, and f_i is the generalized force in the direction of q_i.

The total kinetic energy of the system can be expressed as:

$$V = \frac{1}{2}m_1\left(\dot{x}_1^2 + \dot{y}_1^2\right) + \frac{1}{2}m_2\left(\dot{x}_2^2 + \dot{y}_2^2\right) + \frac{1}{2}m_3\left(\dot{x}_3^2 + \dot{y}_3^2\right) + \frac{1}{2}m_4\left(\dot{x}_4^2 + \dot{y}_4^2\right) + \frac{1}{2}m_5\left(\dot{x}_5^2 + \dot{y}_5^2\right), \tag{2}$$

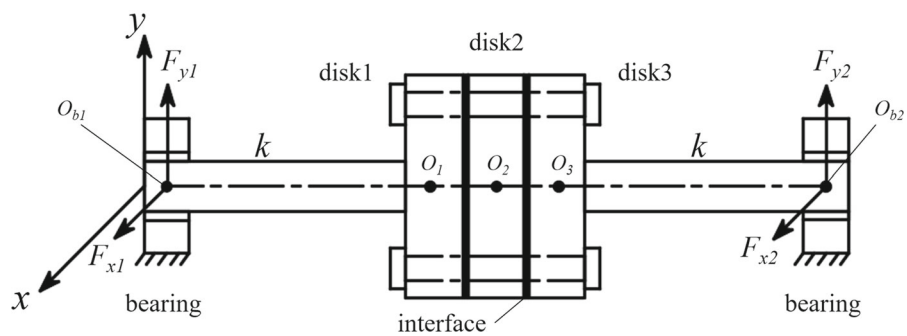

Fig. 2 The rod-fastened rotor model

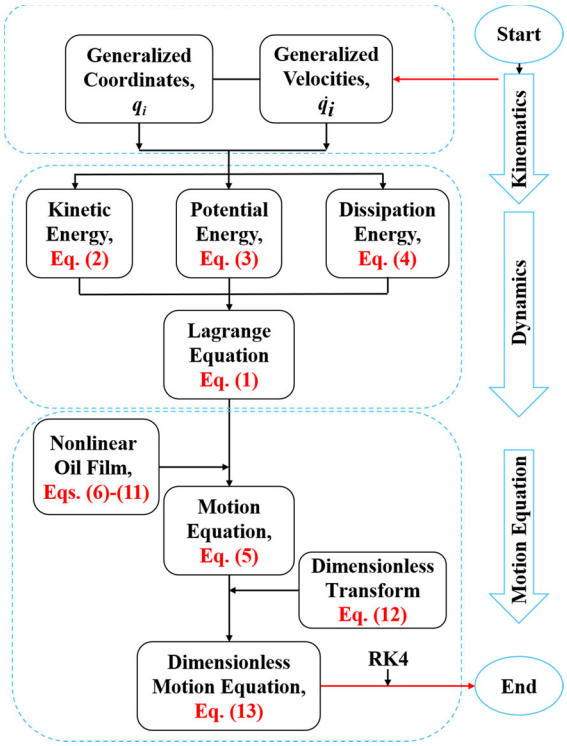

Fig. 4 The flowchart of deriving the equation of motion

The total potential energy of the system is generated as a result of the elastic deformation of rotor as well as the gravity [41], which can be expressed as:

$$\begin{aligned} U = &\frac{1}{2}k_{\text{shaft}}(x_1 - x_2)^2 + \frac{1}{2}k_{\text{shaft}}(y_1 - y_2)^2 \\ &+ \frac{1}{2}k_{\text{in}}(x_2 - x_3)^2 + \frac{1}{2}k_{\text{in}}(y_2 - y_3)^2 + \frac{1}{2}k_{\text{in}}(x_3 - x_4)^2 \\ &+ \frac{1}{2}k_{\text{in}}(y_3 - y_4)^2 + \frac{1}{2}k_{\text{shaft}}(x_4 - x_5)^2 \\ &+ \frac{1}{2}k_{\text{shaft}}(y_4 - y_5)^2 + m_1 g y_1 + m_2 g y_2 + m_3 g y_3 \\ &+ m_4 g y_4 + m_5 g y_5, \end{aligned} \tag{3}$$

The total dissipation energy of the system can be expressed as:

$$\begin{aligned} D = &\frac{1}{2}c_1^2(\dot{x}_1^2 + \dot{y}_1^2) + \frac{1}{2}c_2^2(\dot{x}_2^2 + \dot{y}_2^2) \\ &+ \frac{1}{2}c_3^2\left[(\dot{x}_2 - \dot{x}_3)^2 + (\dot{y}_2 - \dot{y}_3)^2\right] + \frac{1}{2}c_2^2(\dot{x}_3^2 + \dot{y}_3^2) \\ &+ \frac{1}{2}c_3^2\left[(\dot{x}_3 - \dot{x}_4)^2 + (\dot{y}_3 - \dot{y}_4)^2\right] + \frac{1}{2}c_2^2(\dot{x}_4^2 + \dot{y}_4^2) \\ &+ \frac{1}{2}c_3^2\left[(\dot{x}_4 - \dot{x}_5)^2 + (\dot{y}_4 - \dot{y}_5)^2\right] + \frac{1}{2}c_1^2(\dot{x}_5^2 + \dot{y}_5^2), \end{aligned} \tag{4}$$

Taking $q_i = (x_1, y_1, x_2, y_2, x_3, y_3, x_4, y_4, x_5, y_5)^{\mathrm{T}}$ and substituting Eqs. (2)–(4) into Eq. (1), the equation of motion can be expressed as:

$$\begin{cases} m_1\ddot{x}_1 + c_1\dot{x}_1 + k_{\text{shaft}}(x_1 - x_2) = F_{x1} \\ m_1\ddot{y}_1 + c_1\dot{y}_1 + k_{\text{shaft}}(y_1 - y_2) = F_{y1} - m_1 g \\ m_2\ddot{x}_2 + c_2\dot{x}_2 + c_3(\dot{x}_2 - \dot{x}_3) + k_{\text{in}}(x_2 - x_3) = m_2 e_1 \omega^2 \cos(\omega t + \varphi_1) \\ m_2\ddot{y}_2 + c_2\dot{y}_2 + c_3(\dot{y}_2 - \dot{y}_3) + k_{\text{in}}(y_2 - y_3) = m_2 e_1 \omega^2 \sin(\omega t + \varphi_1) - m_2 g \\ m_3\ddot{x}_3 + c_2\dot{x}_3 + c_3(\dot{x}_3 - \dot{x}_4) + k_{\text{in}}(x_3 - x_4) = m_3 e_2 \omega^2 \cos(\omega t + \varphi_2) \\ m_3\ddot{y}_3 + c_2\dot{y}_3 + c_3(\dot{y}_3 - \dot{y}_4) + k_{\text{in}}(y_3 - y_4) = m_3 e_2 \omega^2 \sin(\omega t + \varphi_2) - m_3 g \\ m_4\ddot{x}_4 + c_2\dot{x}_4 + c_3(\dot{x}_4 - \dot{x}_5) + k_{\text{in}}(x_4 - x_5) = m_4 e_3 \omega^2 \cos(\omega t + \varphi_3) \\ m_4\ddot{y}_4 + c_2\dot{y}_4 + c_3(\dot{y}_4 - \dot{y}_5) + k_{\text{in}}(y_4 - y_5) = m_4 e_3 \omega^2 \sin(\omega t + \varphi_3) - m_4 g \\ m_5\ddot{x}_5 + c_2\dot{x}_5 + k_{\text{shaft}} x_5 = F_{x2} \\ m_5\ddot{y}_5 + c_2\dot{y}_5 + k_{\text{shaft}} y_5 = F_{y2} - m_5 g \end{cases} \tag{5}$$

where e_i (i = 1, 2, 3) is the eccentric distance of the rotor, φ_i (i = 1, 2, 3) is the phase angle of mass eccentricity, and F_{x1}, F_{y1}, F_{x2}, and F_{y2} are the nonlinear oil film forces in the x direction and y direction.

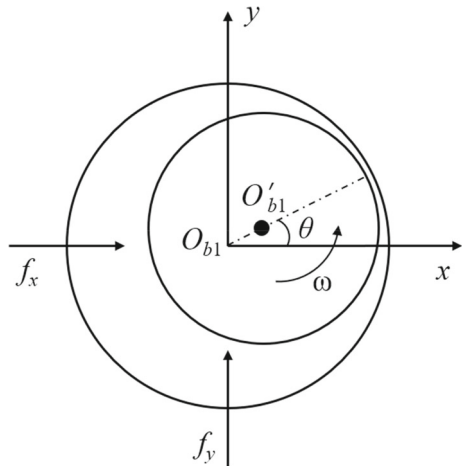

Fig. 5 Model of the nonlinear oil film force

Table 1 The parameters of the rod-fastened rotor

Parameters	Value
Lumped mass m_1/kg	4
Lumped mass m_2/kg	24
Lumped mass m_3/kg	24
Lumped mass m_4/kg	24
Lumped mass m_5/kg	4
Stiffness of shaft k_{shaft}/(N/m)	2.5×10^7
Bending stiffness of interface k_{in}/(Nm/rad)	1.0×10^8
Damping of bearing c_1/(Ns/m)	2100
Damping of disc c_2/(Ns/m)	3500
Damping of interface c_3/(Ns/m)	1050
Eccentric distance of disc e_1, e_2, e_3/mm	0.05
Eccentric phase φ_1, φ_2, φ_3/rad	0
Bearing radius R/mm	48
Bearing length L_b/mm	25
Bearing clearance c/mm	0.18
Lubricant viscosity μ/(Pa s)	0.018

2.2 Nonlinear oil film force

The sliding bearing, which is provided in the design to the supporting rotor, is a main nonlinear source of vibration with strong nonlinearity. The model of the nonlinear oil film force model is shown in Fig. 5.

The Capone nonlinear oil film force model [42] is applied to illustrate the oil film force of the sliding bearing. The oil film force can be expressed as Eq. (6) when the lubricating oil meets the following conditions:

1. The lubricating oil is an isothermal, laminar flow incompressible fluid.
2. The lubricant dynamic viscosity is constant.

$$\begin{pmatrix} f_x \\ f_y \end{pmatrix} = \frac{1}{\delta P_f} \begin{Bmatrix} F_{bx} \\ F_{by} \end{Bmatrix}, \tag{6}$$

where δ is the Sommerfeld correction coefficient, and $\delta = (\eta\omega RL/P_f) \cdot (R/c)^2 \cdot (L/2R)^2$. P_f is the external mass of the bearing. In this paper, P_f is the half of mass of rotor, P_f = 40 kg.

$$\begin{aligned} F_{bx} &= -\frac{\left[(X-2\dot{Y})^2+(Y+2\dot{X})^2\right]^{1/2}(3XV-\sin\alpha G-2\cos\alpha S)}{1-X^2-Y^2} \\ F_{by} &= -\frac{\left[(X-2\dot{Y})^2+(Y+2\dot{X})^2\right]^{1/2}(3YV+\cos\alpha G-2\sin\alpha S)}{1-X^2-Y^2}, \end{aligned} \tag{7}$$

where $X = x/c$, $Y = y/c$, c is the bearing clearance, and V, S, G, and α can be expressed as:

$$V = \frac{2+(Y\cos\alpha - X\sin\alpha)\times G}{1-X^2-Y^2}, \tag{8}$$

$$S = \frac{X\cos\alpha + Y\sin\alpha}{1-(X\cos\alpha + Y\sin\alpha)^2}, \tag{9}$$

$$G = \frac{2\left[\frac{\pi}{2}+\arctan\frac{Y\cos\alpha - X\sin\alpha}{(1-X^2-Y^2)^{1/2}}\right]}{(1-X^2-Y^2)^{1/2}}, \tag{10}$$

$$\begin{aligned} \alpha = &\arctan\frac{Y+2\dot{X}}{X-2\dot{Y}} - \frac{\pi}{2}\operatorname{sign}\left[\frac{Y+2\dot{X}}{X-2\dot{Y}}\right] \\ &-\frac{\pi}{2}\operatorname{sign}(Y+2\dot{X}), \end{aligned} \tag{11}$$

2.3 Dimensionless transform of the equation of motion

The dimensionless transform of the equation of motion is given as Eq. (12).

$$X_i = \frac{x_i}{c}, \quad Y_i = \frac{y_i}{c}, \quad \tau = \omega t, \tag{12}$$

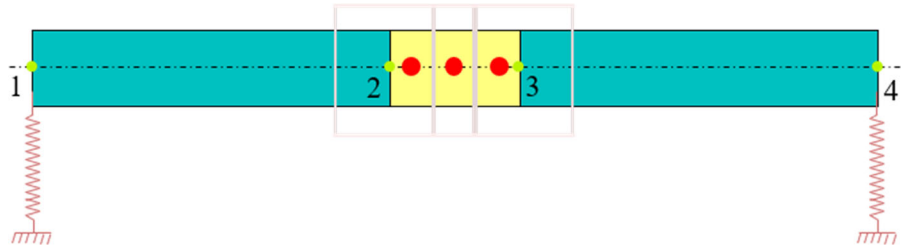

Fig. 6 The modal structure of the rotor [22, 23]

Table 2 The modal result

	Result in this paper	SAMCEF result	Relative error/%
1st natural frequency/Hz	313.40	318.33	1.55
2nd natural frequency/Hz	1343.33	1387.88	3.21
3rd natural frequency/Hz	2611.49	2761.73	5.44

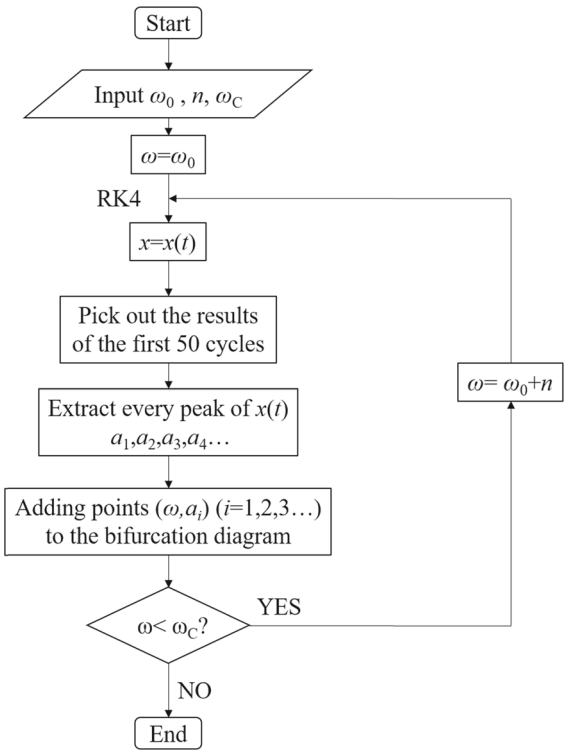

Fig. 7 The flowchart for bifurcation diagram

Substituting Eq. (12) into Eq. (5), the dimensionless equation of motion can be expressed as:

$$\begin{cases}
\ddot{X}_1+\frac{c_1}{m_1\omega}\dot{X}_1+\frac{k_{\text{shaft}}}{m_1\omega^2}(X_1-X_2)=\frac{F_{x1}}{m_1c\omega^2}\\
\ddot{Y}_1+\frac{c_1}{m_1\omega}\dot{Y}_1+\frac{k_{\text{shaft}}}{m_1\omega^2}(Y_1-Y_2)=\frac{F_{y1}}{m_1c\omega^2}-\frac{g}{c\omega^2}\\
\ddot{X}_2+\frac{c_2}{m_2\omega}\dot{X}_2+\frac{c_3}{m_2\omega}(\dot{X}_2-\dot{X}_3)+\frac{k_{\text{in}}}{m_2\omega^2}(X_2-X_3)=\frac{e_1}{c}\cos(\tau+\varphi_1)\\
\ddot{Y}_2+\frac{c_2}{m_2\omega}\dot{Y}_2+\frac{c_3}{m_2\omega}(\dot{Y}_2-\dot{Y}_3)+\frac{k_{\text{in}}}{m_2\omega^2}(Y_2-Y_3)=\frac{e_1}{c}\sin(\tau+\varphi_1)-\frac{g}{c\omega^2}\\
\ddot{X}_3+\frac{c_2}{m_3\omega}\dot{X}_3+\frac{c_3}{m_3\omega}(\dot{X}_3-\dot{X}_4)+\frac{k_{\text{in}}}{m_3\omega^2}(X_3-X_4)=\frac{e_2}{c}\cos(\tau+\varphi_2)\\
\ddot{Y}_3+\frac{c_2}{m_3\omega}\dot{Y}_3+\frac{c_3}{m_3\omega}(\dot{Y}_3-\dot{Y}_4)+\frac{k_{\text{in}}}{m_3\omega^2}(Y_3-Y_4)=\frac{e_2}{c}\sin(\tau+\varphi_2)-\frac{g}{c\omega^2}\\
\ddot{X}_4+\frac{c_2}{m_3\omega}\dot{X}_4+\frac{c_3}{m_3\omega}(\dot{X}_4-\dot{X}_5)+\frac{k_{\text{in}}}{m_3\omega^2}(X_4-X_5)=\frac{e_3}{c}\cos(\tau+\varphi_3)\\
\ddot{Y}_4+\frac{c_2}{m_4\omega}\dot{Y}_4+\frac{c_3}{m_4\omega}(\dot{Y}_4-\dot{Y}_5)+\frac{k_{\text{in}}}{m_4\omega^2}(Y_4-Y_5)=\frac{e_3}{c}\sin(\tau+\varphi_3)-\frac{g}{c\omega^2}\\
\ddot{X}_5+\frac{c_2}{m_5\omega}\dot{X}_5+\frac{k_{\text{shaft}}}{m_5\omega^2}X_5=\frac{F_{x2}}{m_5c\omega^2}\\
\ddot{Y}_5+\frac{c_2}{m_5\omega}\dot{Y}_5+\frac{k_{\text{shaft}}}{m_5\omega^2}Y_5=\frac{F_{y2}}{m_5c\omega^2}-\frac{g}{c\omega^2}
\end{cases} \tag{13}$$

2.4 Numerical method

It can be known from Eqs. (6)–(11). The expression of oil film force contains X, Y, X^2, Y^2 and arctan$(Y+2X)$ et al. Hence, Eq. (13) has a strong nonlinear characteristic. In this paper, the fourth-order Runge–Kutta method [43, 44] is employed to solve Eq. (13).

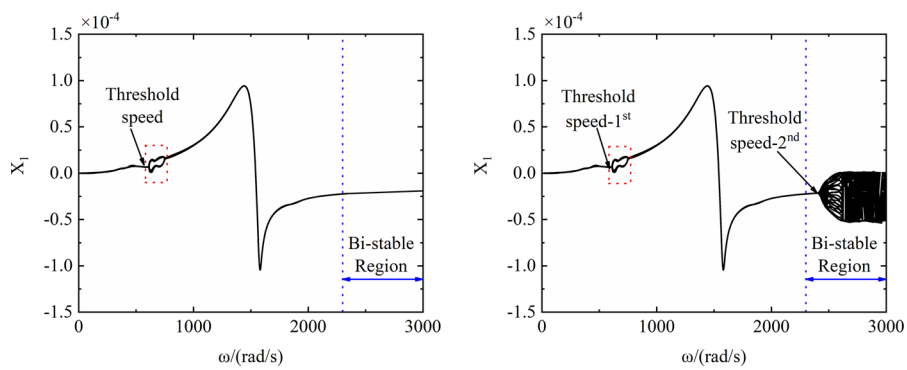

(a) Acceleration progress **(b)** Deceleration progress

Fig. 8 The bifurcation diagram of X_1 without damping of the interface

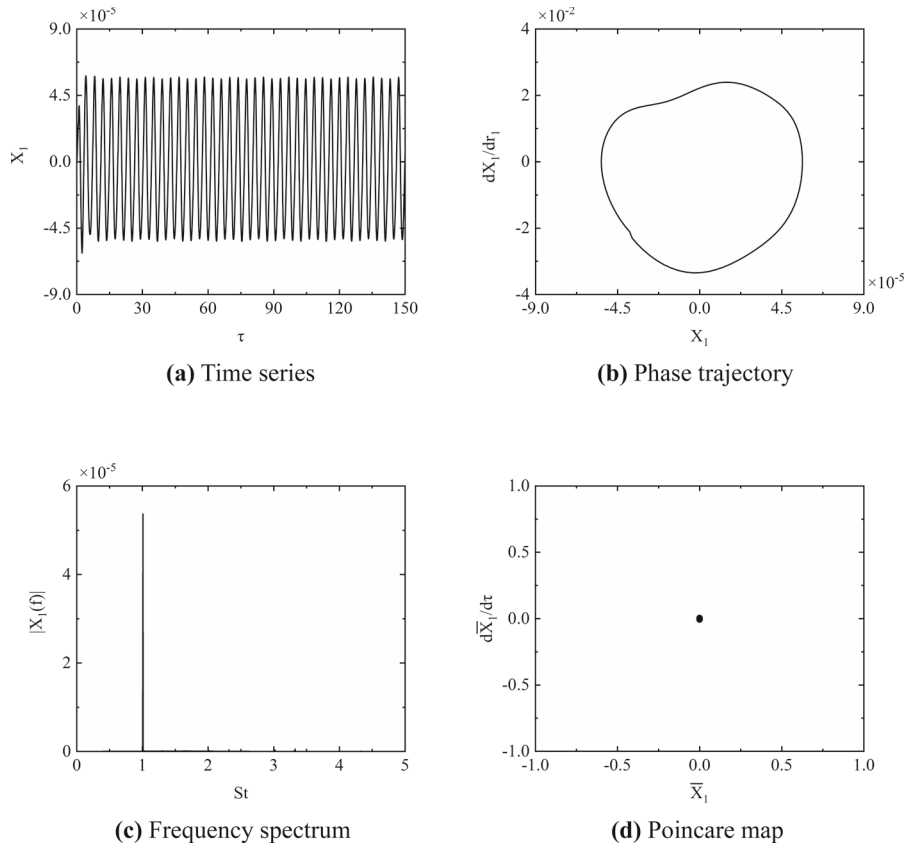

(a) Time series **(b)** Phase trajectory

(c) Frequency spectrum **(d)** Poincare map

Fig. 9 Numerical analysis results at ω = 400 rad/s

3 Numerical simulation result

The parameters of the rod-fastened rotor-bearing system are shown in Table 1. To verify the model, the first three-order natural frequencies of the rotor are calculated by eigenvalue analysis. The results are, respectively, 313.40, 1343.33, 2611.49 Hz. Meanwhile, the natural frequencies of this model are calculated by the business software SAMCEF. It should be noted that in the process of modelling, the shaft is simplified as a massless elastic shaft, and the discs are simplified as concentrated masses. The two adjacent discs were connected by a bearing unit, and the bending stiffness of the bearing was 1.0×10^8 Nm/rad. The modelling structure of the rotor is shown in Fig. 6. The results of natural frequencies are shown in Table 2. The relative error is small, and the program of this paper can be used in further nonlinear research.

The nonlinear dynamic behaviour of the system is determined by the fourth-order Runge–Kutta method and implemented in MATLAB. The bifurcation diagram, time series, phase trajectory, frequency domain and Poincare map are given to illustrate the nonlinear characteristics of the system.

3.1 Stability behaviour

The phenomenon of the difference of the dynamic behaviour during acceleration and deceleration is called bistable behaviour. In this section, the bifurcation diagrams during acceleration and deceleration are calculated to explore this behaviour. The flowchart for bifurcation diagram is shown in Fig. 7.

Based on the assumption 1 and the national standard of China (Ref. [45]), when the rotating speed does not exceed 942 rad/s (9000 rpm), the displacement signal of bearing must be paid special attention to. So, the X_1 is chosen for stability analysis.

Figure 8a is the bifurcation diagram of X_1 during acceleration without damping of the interface. When the rotating speed is low, i.e. $\omega < 614$ rad/s, the system maintains periodic-1 motion, and the main excitation source is the imbalance of the rotor.

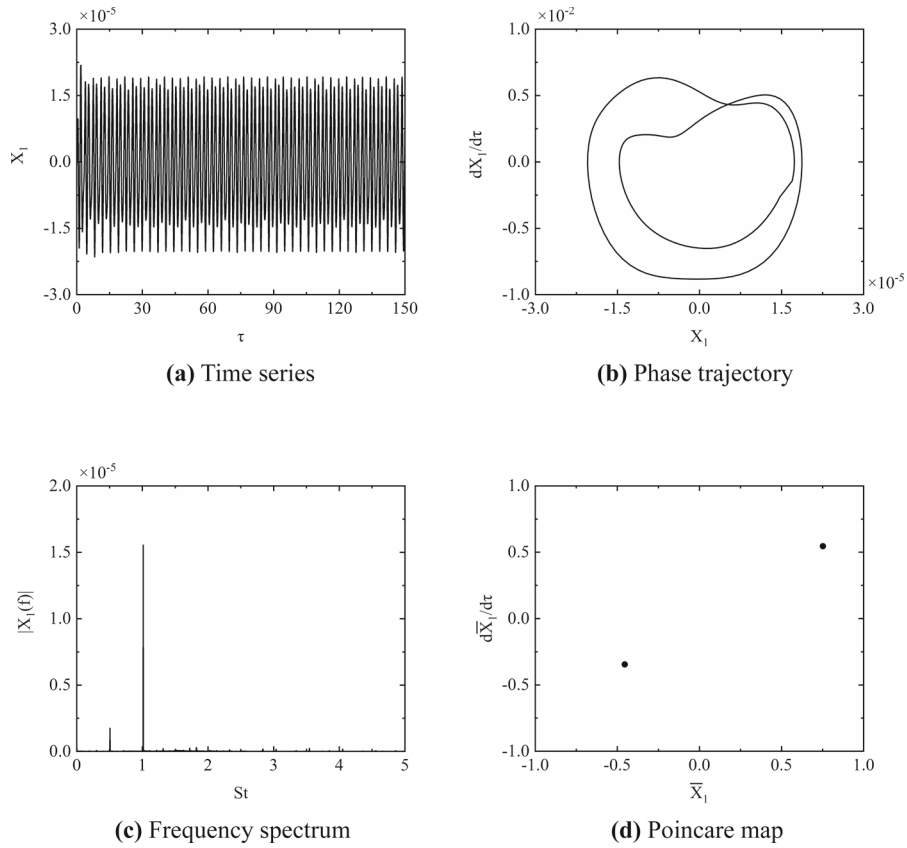

(a) Time series **(b)** Phase trajectory

(c) Frequency spectrum **(d)** Poincare map

Fig. 10 Numerical analysis results at ω = 700 rad/s

Figure 9 is the numerical solution of the rotor with ω = 400 rad/s, where there is a closed loop in Fig. 9b and one isolated point in Fig. 9d.

It should be noted that the dimensionless frequency *St* is introduced to simplify the frequency analysis: $St = f/f_n$, where $f_n = n/60$. Because the time series of X_1 are different during acceleration and deceleration, the horizontal and vertical coordinates of X_1 are different too. Therefore, unifying the horizontal and vertical coordinates of Poincaré diagram under different conditions would make the motion analysis more intuitive. Based on the method in [46], the $\overline{X}_1$ is applied to ensure that the horizontal and vertical coordinates of Poincaré map are in the range of [− 1, 1], $\overline{X}_1 = X_1/X_{1(\max)}$.

The system enters periodic-2 motion at $614 < \omega < 768$ rad/s. The numerical solution of the rotor at ω = 700 rad/s is shown in Fig. 10. The main vibration occurs at St = 1/2 and St = 1, which indicates that the main excitation source is the nonlinear oil film force and imbalance of the rotor. With increasing rotating speed, the system returns to periodic-1 motion when $\omega > 768$ rad/s.

Figure 8b is the bifurcation diagram of X_1 during deceleration without damping of the interface. The bifurcation behaviour is the same as its counterpart of acceleration when $\omega < 2358$ rad/s. When the rotating speed exceeds 2358 rad/s, the system passes through quasiperiodic motion at $2358 < \omega < 2606$ rad/s and chaotic motion at $\omega > 2786$ rad/s. This progress is different from the progress in Fig. 8a. Figure 11 is the numerical result at ω = 2600 rad/s. The phase trajectory presents one closed loop during acceleration and a series of closed loops during deceleration. There is one isolated point during acceleration and a closed loop during deceleration. When the rod-fastened rotor accelerates, the system maintains periodic-1 motion, and when the rotor decelerates, the system maintains quasiperiodic motion. Figure 12 is the numerical analysis result at ω = 3000 rad/s under acceleration and deceleration conditions. When the rod-fastened rotor accelerates, the system maintains periodic-1 motion, and when it decelerates, the system maintains

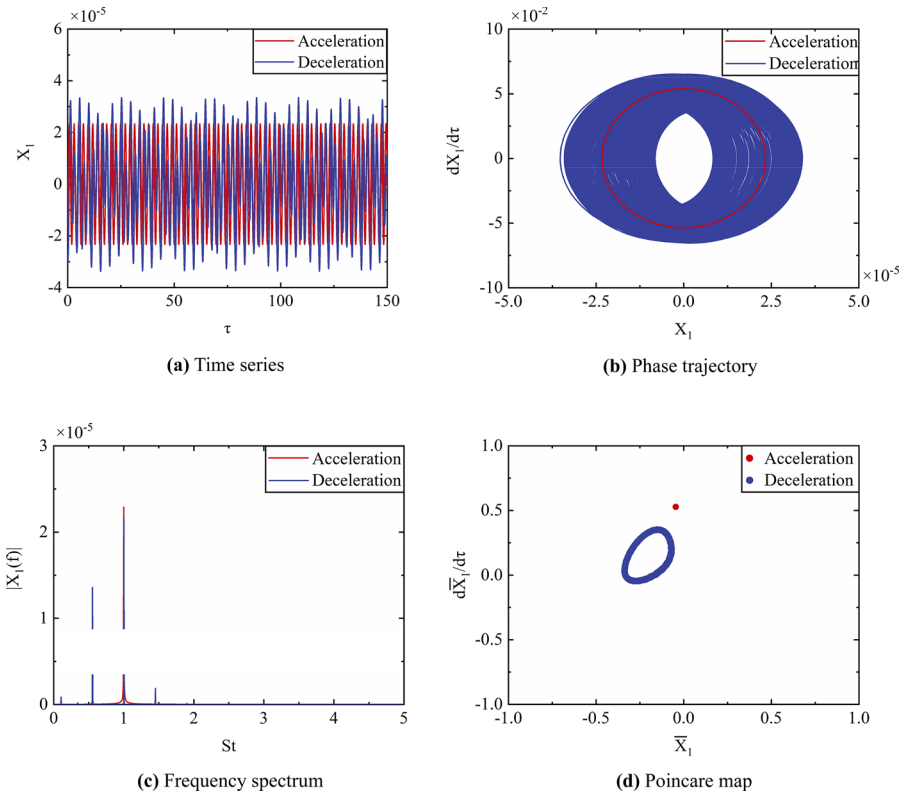

Fig. 11 Numerical analysis results at ω = 2600 rad/s

chaotic motion, and the chaotic motion contains three strange attractors.

Figure 13a is the bifurcation diagram of X_1 during acceleration with damping of the interface. This bifurcation behaviour is more complex than the bifurcation behaviour in Fig. 8a. When $\omega < 388$ rad/s, the system maintains periodic-1 motion, and with the increase of rotating speed, the system enters periodic-2 motion at $388 < \omega < 541$ rad/s. The main excitation source is the nonlinear oil film force and imbalance of the rotor, which are the same as the periodic-2 motion in Fig. 8a, b. With increasing rotating speed, the system returns to periodic-1 motion at $384 < \omega < 1472$ rad/s. The system bifurcates to periodic-2 motion at ω = 2420 rad/s and then to periodic-4 motion at ω = 2807 rad/s.

Figure 13b is the bifurcation diagram of X_1 during deceleration with damping of the interface. When $\omega < 2324$ rad/s, the bifurcation behaviour is the same as that of its counterpart in Fig. 13a. When $\omega > 2324$ rad/s, the system passes through quasiperiodic motion and chaotic motion in turn. Figure 14 shows the numerical result at ω = 2700 rad/s under acceleration and deceleration conditions. The phase trajectory presents two closed loops while accelerating and a series of closed loops while decelerating. There are two peaks while accelerating and a frequency band while decelerating. This proves that the system maintains periodic-2 motion under acceleration and quasiperiodic motion during deceleration. Figure 15 shows the numerical result at ω = 2900 rad/s under acceleration and deceleration conditions. This numerical result can provide evidence that the system maintains perodic-4 motion when accelerating and chaotic motion when decelerating.

The damping of the interface plays a great role in the bifurcation behaviour. The bifurcation behaviours are arranged in Table 3. When the damping of the interface is considered, there are three instabilities, while there are only two instabilities if the damping of the interface is ignored. Compared with the condition of neglecting damping of the interface, when damping of the interface is considered, the first two unstable speeds increase significantly, the first unstable interval increases, and the second unstable interval decreases.

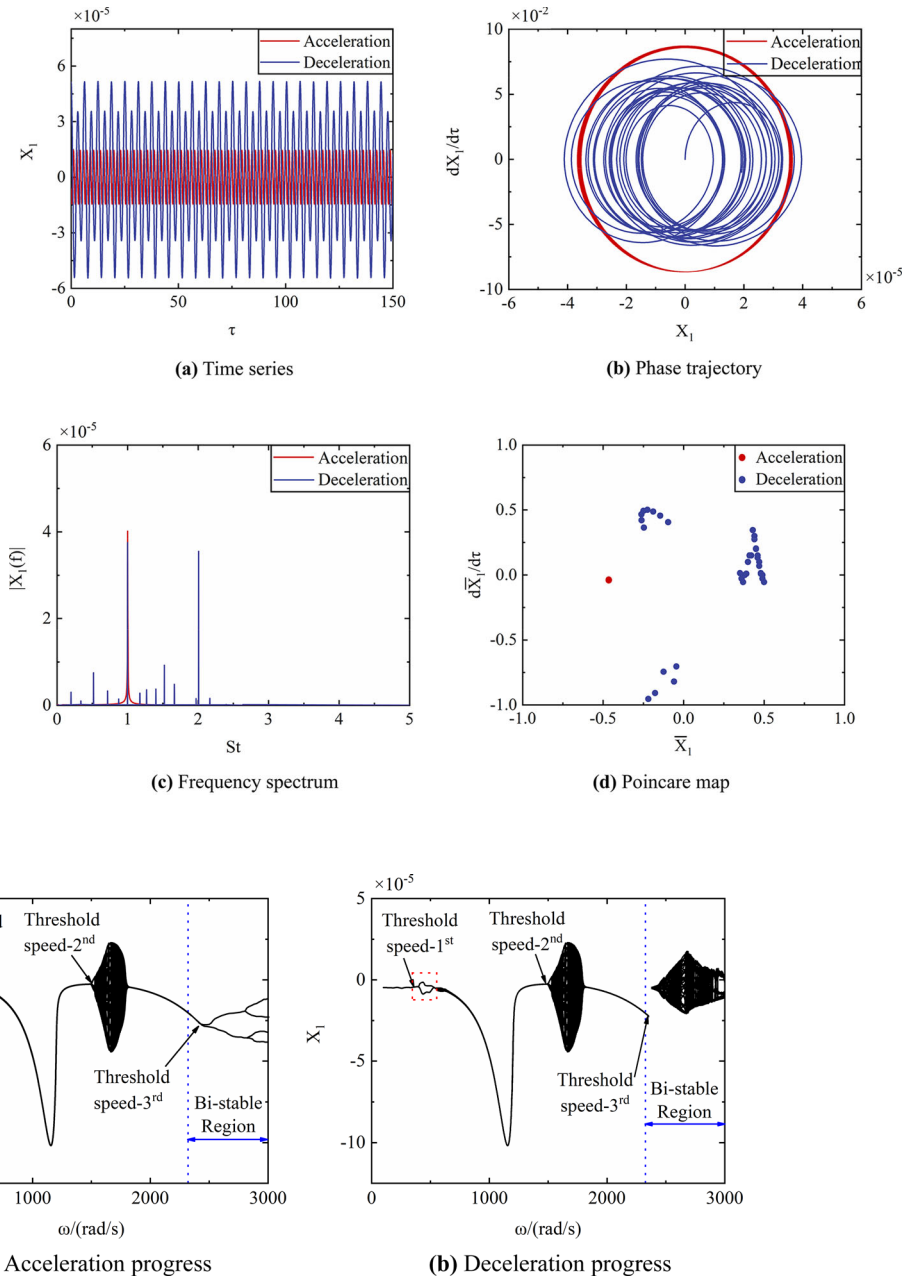

Fig. 12 Numerical analysis results at ω = 3000 rad/s

Fig. 13 The bifurcation diagram of X_1 with damping of the interface

3.2 Transient response

To investigate the bistable behaviour of the rod-fastened rotor-bearing system, the transient response without damping of the interface is shown in Fig. 16a, and the transient response with damping of the interface is shown in Fig. 16b.

There is an amplitude in the region of $614 < \omega < 768$ rad/s. With increasing rotating speed, the displacement increases gradually. The displacement curve during the deceleration is also shown in this figure. This curve is the same as the curve of acceleration in the region of $\omega < 2358$ rad/s. When $\omega > 2358$ rad/s, the vibration displacement of the

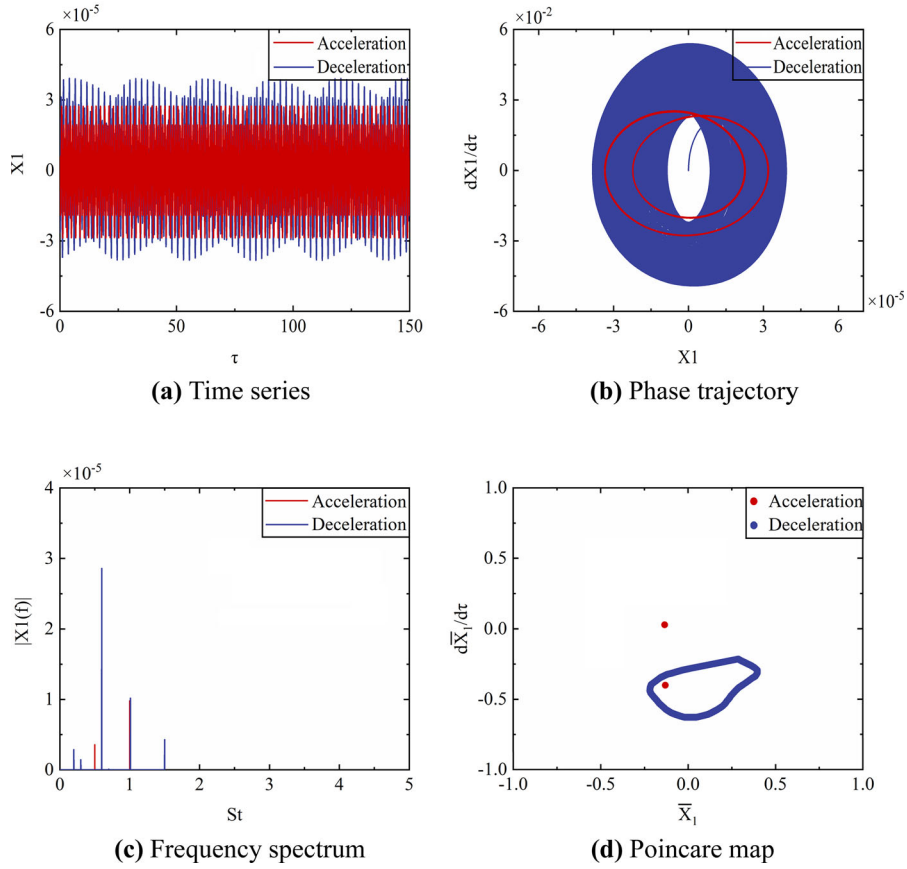

Fig. 14 Numerical analysis results at ω = 2700 rad/s

system decreases gently with decreasing rotating speed. When the rotating speed is close to 2358 rad/s, the hysteretic cycle occurs, and the displacement of the system decreases rapidly over a very small interval. The bistable region is at $\omega > 2358$ rad/s, the periodic-2 motion region is at $614 < \omega < 768$ rad/s, and the jumping rotating speed is ω = 2358 rad/s. These behaviours are identical to their counterparts in Sect. 2.1.

Figure 16b is the vibration curve of the rotor with the damping of the interface. This curve is like the curve in Fig. 16a. The periodic-2 motion region is at $388 < \omega < 541$ rad/s, the bistable region is at $\omega > 1472$ rad/s, and the jumping rotating speed is ω = 1472 rad/s. In addition, there is a slight difference in that when the damping of the interface is considered, the curve of the displacement is steeper during the hysteretic cycle.

3.3 Sensitivity analysis

Taking the damping of discs, damping of interface and damping of bearing as the uncertain parameters. The fluctuating values of uncertain parameters are 10%. The sampling results of uncertain parameters are shown in Table 4.

The rotating speed at which bistable phenomena occur, ω_{n1}, is calculated. The multinomial expansion of ω_{n1} for uncertain parameters is obtained.

$$\omega_{n1} = 780.97 - 0.2\xi_1 - 1.12\xi_2 + 0.973\xi_3, \qquad (14)$$

where ξ_1, ξ_2, ξ_3 are the standard normal distribution samples of damping of disc, damping of interface and damping of bearing, respectively. The sensitivity analysis is shown in Fig. 17, based on the method proposed in literature [47].

It can be known that the sensitivity of damping of discs to ω_{n1} is very small, which means that ω_{n1} is almost constant with the changes of the damping of

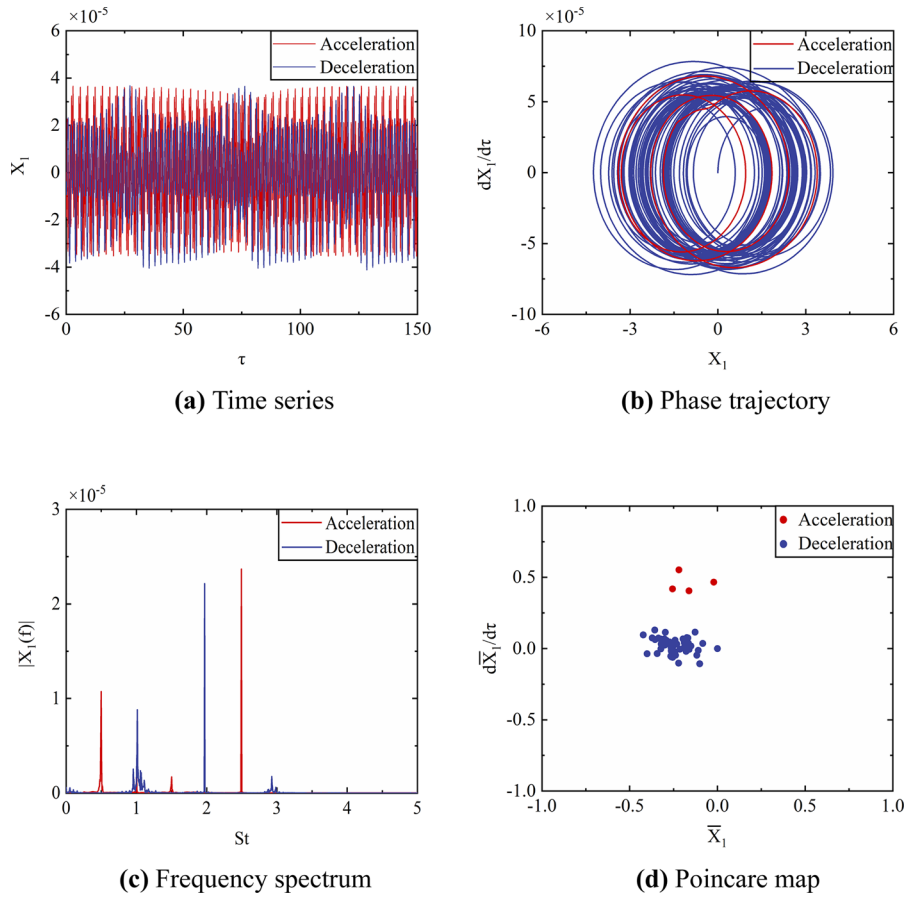

Fig. 15 Numerical analysis results at ω = 2900 rad/s

Table 3 Nonlinear behaviours of rotor

Type	Condition	Instability time	1st threshold speed/(rad/s)	2nd threshold speed/(rad/s)	3rd threshold speed/(rad/s)	Nonlinear Behaviour	Bistable Region/(rad/s)
Without interface damping	Acceleration	1	614	–	–	P-1 → P-2 → P-1	2358–3000
	Deceleration	2	614	2358	–	P-1 → P-2 → P-1 → P-qua → Chaotic	
With interface damping	Acceleration	3	388	1472	2420	P-1 → P-2 → P-1 → P-qua → P-1 → P-2 → P-4	2324–3000
	Deceleration	3	388	1472	2324	P-1 → P-2 → P-1 → P-qua → P-1 → P-qua → Chaotic	

discs. The sensitivity of damping of interface to ω_{n1} is − 0.7481, which means that the ω_{n1} decrease with the decrease of damping of interface. The sensitivity of damping of bearing to ω_{n1} is 0.6499, which means that the ω_{n1} increases with the decrease of damping of bearing. Hence, the effects of damping of interface and bearing on ω_{n1} should be noted.

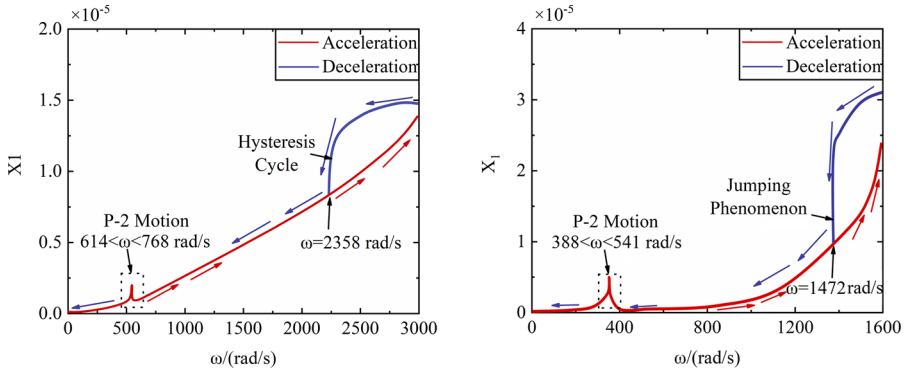

(a) Without damping of the interface **(b)** With damping of the interface

Fig. 16 Transient response of X_1

Table 4 Sampling result

	Damping of disc/(Ns/m)	Damping of interface/(Ns/m)	Damping of bearing/(Ns/m)
1	2310	1155	3850
2	2310	1155	3150
3	2310	945	3850
4	2310	945	3150
5	1890	1155	3850
6	1890	1155	3150
7	1890	945	3850
8	1890	945	3150

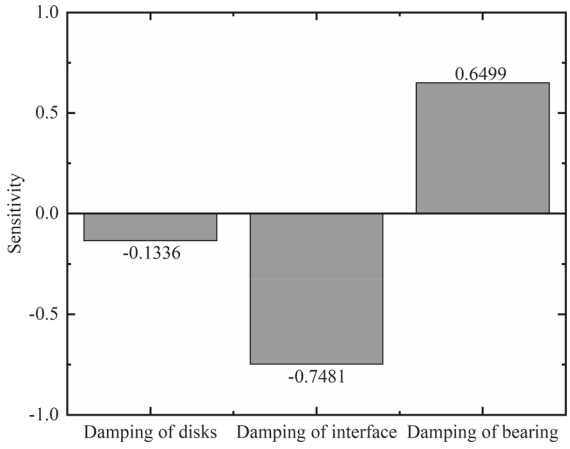

Fig. 17 Sensitivity analysis results

4 Rod-fastened rotor-bearing bench

A rod-fastened rotor-bearing bench is set up to verify the bistable behaviour revealed in Chapter 2. The structure of the rod-fastened rotor is shown in Fig. 18.

This rotor contains 9 compressor discs, 3 turbine discs and a torque tube. All discs and the torque tube are fixed together by eight rods, which are evenly distributed across the circumferential direction. The maximum axial length is 1077 mm, the maximum diameter is 172 mm, the rod diameter is 12 mm, the material of the discs and torque tube is 1Cr11Ni2W2-MoV, and the material of the rods is GH4169. The main material properties are shown in Table 5.

4.1 The dynamic parameter of the rod-fastened rotor

Based on the finite element method, the dynamic parameter of the rod-fastened rotor is calculated. In the calculation process, the damping property of the oil film force is ignored, only the stiffness is considered, and the rod is omitted. The effect of the preload is simplified to the bending spring of the interface [16, 48–50]. According to our previous study [20, 51], when the preload is 8 kN, the bending stiffness of the spring is 1.5×10^9 Nm/rad. The relation between the

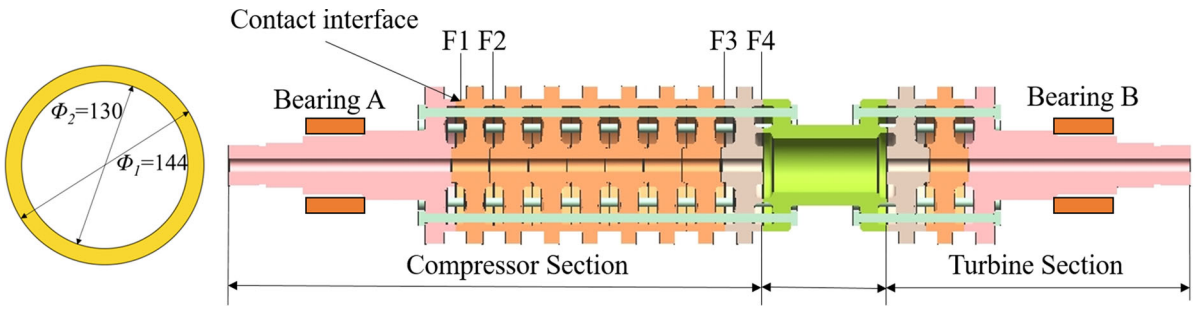

Fig. 18 Rod-fastened rotor model for the test

Table 5 Material properties

	1Cr11Ni2W2MoV	GH4169
Density/(kg/m^3)	7800	8240
Young's modulus/Pa	196 × 10^9	204 × 10^9
Shear modulus/Pa	73 × 10^9	79 × 10^9
Poisson's ratio	0.33	0.30

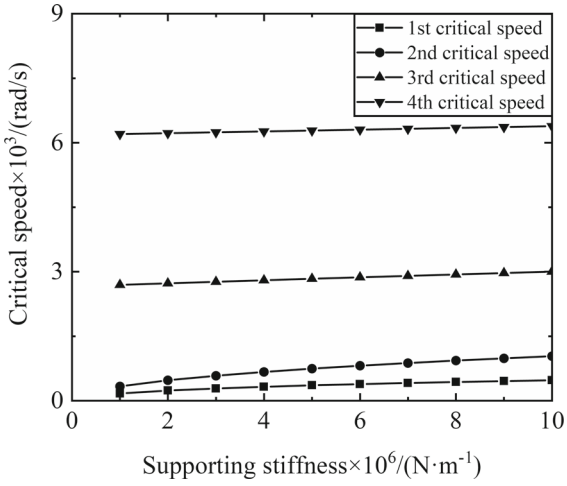

Fig. 19 The relation between the critical speeds and supporting bearing

first four orders of critical speeds and supporting stiffness is shown in Fig. 19.

With increasing stiffness, the first two orders of critical speeds increase rapidly. When the stiffness increases from 1 × 10^6 N/m to 1 × 10^7 N/m, the first-order critical speed increases from 168.76 to 475.15 rad/s, increasing by 181.54%. The second-order critical speed increases from 334.83 to 1036.26 rad/s, increasing by 209.48%. The third-order critical speed and fourth-order critical speed increase slightly, while the stiffness increases from 1 × 10^6 N/m to 1 × 10^7 N/m, and the third-order critical speed increases from 2694.27 to 3002.70 rad/s, increasing by 11.50%. The fourth-order critical speed increases from 6204.59 to 6388.19 rad/s, increasing by 2.95%. Figure 20 shows the first four orders of mode shapes of the rod-fastened rotor-bearing system, with a bearing stiffness of 5 × 10^6 N/m. The first two-order mode shapes are the vibration type of the rigid body, which presents the dynamic behaviour of the bearing, and this vibration is caused by the bearing. The third- and fourth-order mode shapes are bending modes that reveal the dynamic behaviour of the rotor. Hence, with increasing supporting stiffness, the first two orders of critical speeds increase greatly, and the third- and fourth-order critical speeds increase slightly. The dynamic

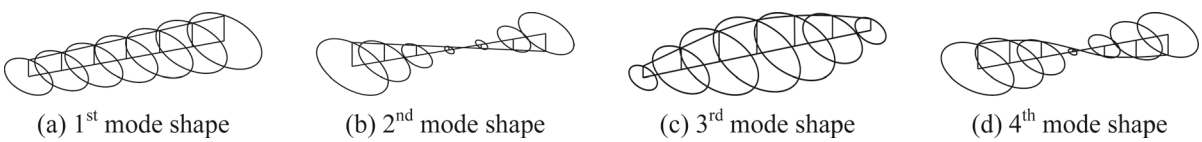

Fig. 20 Mode shape of the rotor

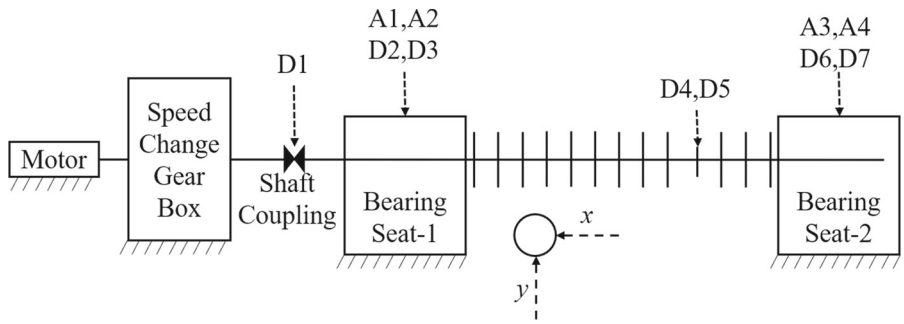

Fig. 21 The schematic diagram of sensor arrangement

Table 6 The main parameters of sensors

Sensor	Main dimensions	Sensitivity	Range	Sensor	Main dimensions	Sensitivity	Range
A1	M5	0.495 mV/m/s^2	30 g	A2	M5	0.522 mV/m/s^2	30 g
A3	M5	0.522 mV/m/s^2	30 g	A4	M5	0.532 mV/m/s^2	30 g
D1	Φ8	12.0 V/mm	2.1 mm	D2	Φ8	12.0 V/mm	2.1 mm
D3	Φ8	12.0 V/mm	2.1 mm	D4	Φ8	10.7 V/mm	3.5 mm
D5	Φ8	10.7 V/mm	3.5 mm	D6	Φ8	12.0 V/mm	3.5 mm
D7	Φ8	10.7 V/mm	3.5 mm	NAN	NAN	NAN	NAN

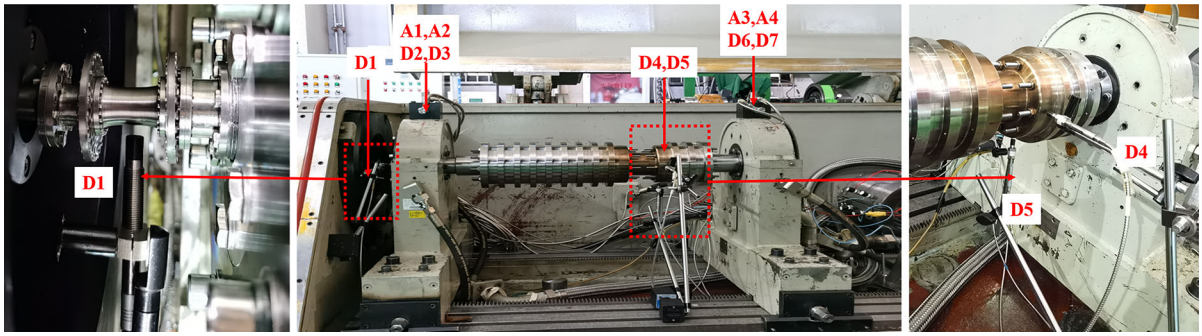

Fig. 22 Rod-fastened rotor-bearing system bench

parameters of the rod-fastened rotor can provide a basis for the experimental research in Sect. 4.

4.2 The arrangement of sensors

The vibration signals of the rotor are collected by seven displacement sensors and four acceleration sensors. The collected signals are transmitted to the DASP data-acquisition instrument and transmitted to the computer through filtering to complete the data storage and online monitoring.

The arrangement of the sensors is shown in Fig. 21, where A1–A4 are acceleration sensors, which are used to monitor the vibration acceleration signal of the horizontal and vertical directions of the bearing seats. A1 and A2 are used to monitor the acceleration signal of bearing seat-1, and A3 and A4 are used to monitor the acceleration signal of bearing seat-2. D1–D7 are displacement sensors that are used to monitor the displacement signal of the horizontal and vertical directions of the rotor. D1 is used to monitor the displacement signal of the shaft coupling to ensure the safety of the experiment, D2 and D3 are used to monitor the displacement signal of bearing seat-1, D4 and D5 are used to monitor the displacement signal of the torque tube, and D6 and D7 are used to monitor the

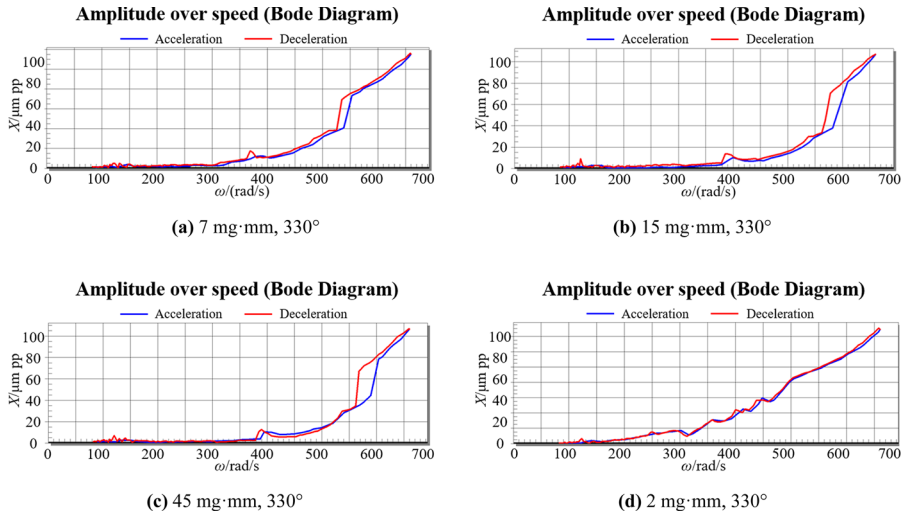

(a) 7 mg·mm, 330° **(b)** 15 mg·mm, 330°

(c) 45 mg·mm, 330° **(d)** 2 mg·mm, 330°

Fig. 23 Vibration curve of the rotor

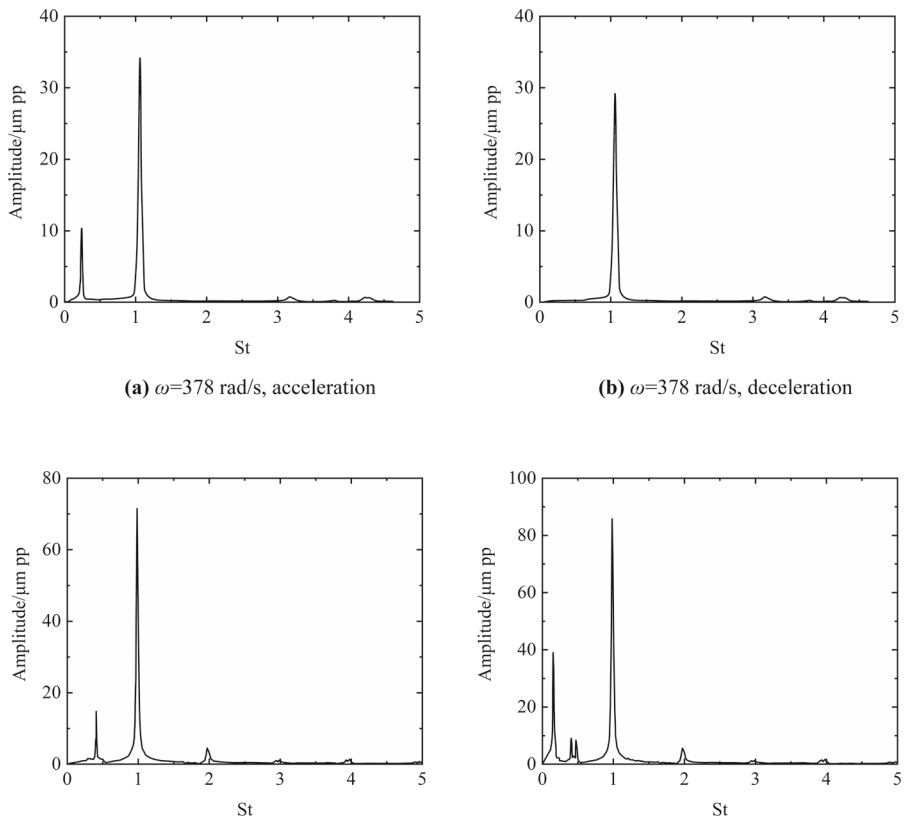

(a) ω=378 rad/s, acceleration **(b)** ω=378 rad/s, deceleration

(c) ω=560 rad/s, acceleration **(d)** ω=560 rad/s, deceleration

Fig. 24 FFT results of rotor

displacement signal of bearing seat-2. All sensors were calibrated by the 304 Institute of Aviation Industry Corporation of China. The major dimensions, sensitivity and measuring range of the sensors are shown in Table 6.

5 Experimental results

The rod-fastened rotor-bearing system was designed and built with the purpose of reproducing and verifying the bistable behaviour and hysteretic cycle

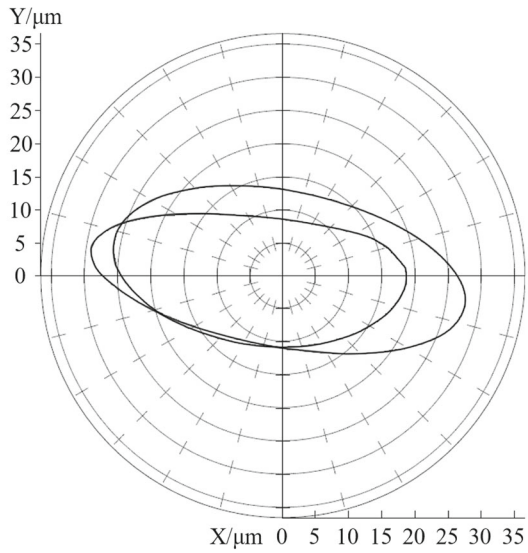

(a) ω=378 rad/s, acceleration

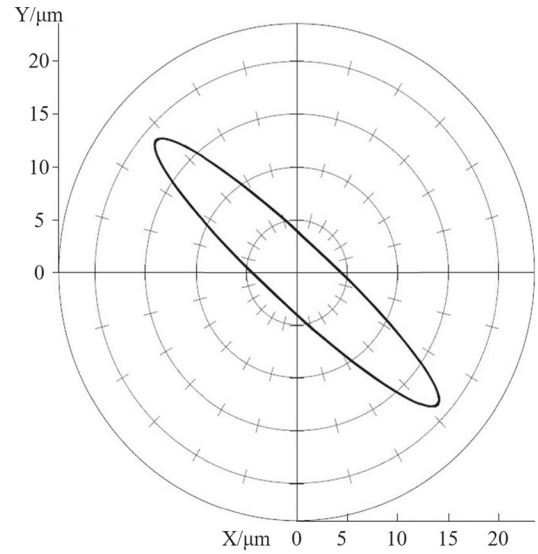

(b) ω=378 rad/s, deceleration

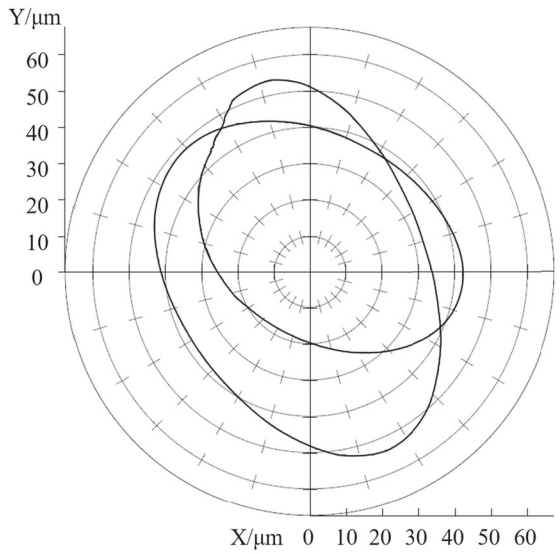

(c) ω=560 rad/s, acceleration

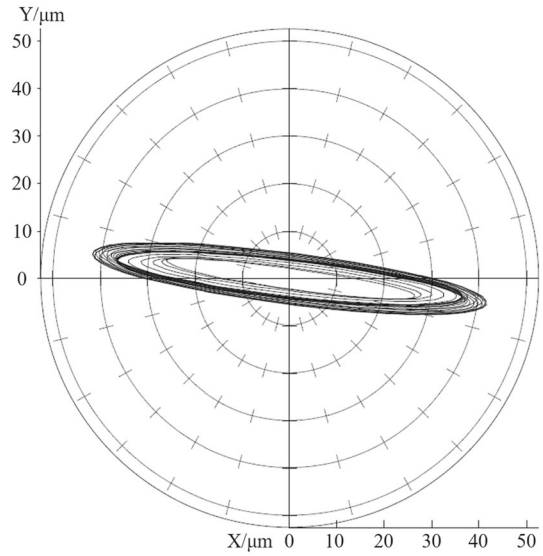

(d) ω=560 rad/s, deceleration

Fig. 25 Orbit results of rotor

of the system (Fig. 22). The foundation is a cast iron of aluminium profiles supporting the rotor, an 80-kW asynchronous motor, a speed variator and a shaft coupling. The maximum rotating speed was designed between the first-order and second-order critical speed of the system at approximately 116 Hz (733 rad/s). Each disc contains 30 threaded drilled holes radially distributed with a radius of 160 mm for rotor balancing. Before beginning the test, the imbalance of the rod-fastened rotor is approximately 7 g mm, and the phase of the imbalance is approximately 330°. The angular acceleration is 15 rad/s^2 during acceleration and 30 rad/s^2 during deceleration.

Fig. 26 Phase space reconstruction

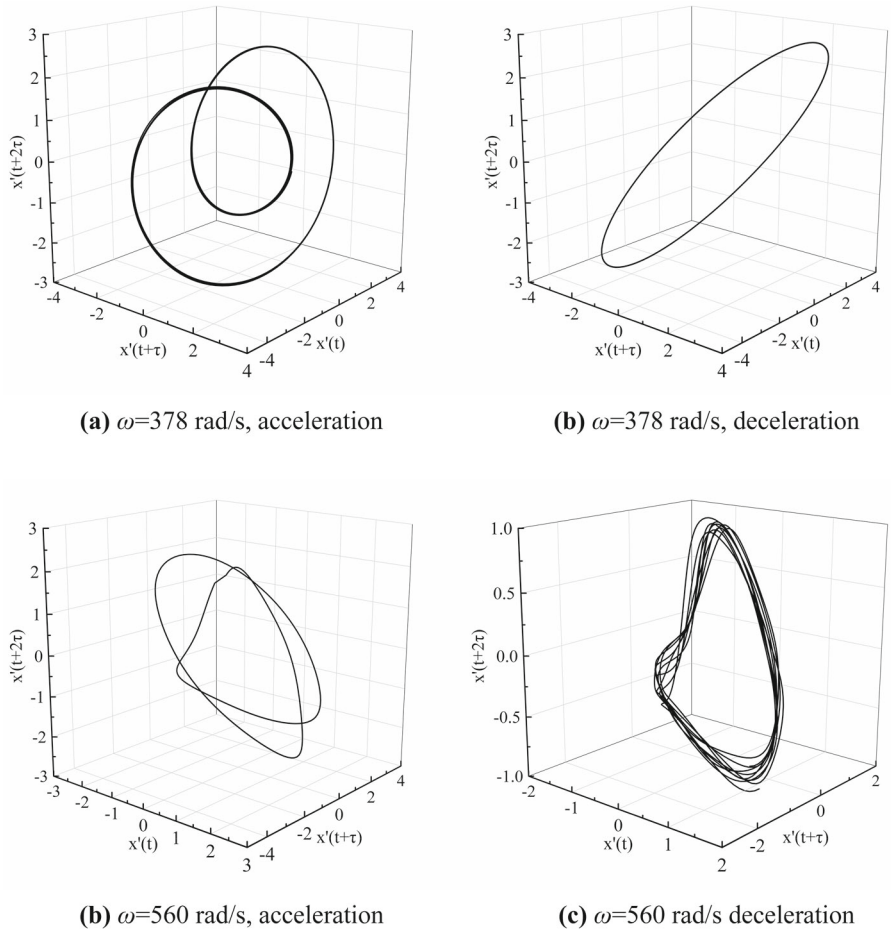

(a) ω=378 rad/s, acceleration

(b) ω=378 rad/s, deceleration

(b) ω=560 rad/s, acceleration

(c) ω=560 rad/s deceleration

Figure 23a is the curve of displacement. It can be known that the bistable behaviour appears in two regions, 366–418 and 555–576 rad/s.

In the first region, there is a peak at 387.46 rad/s during acceleration, while there is no peak during deceleration. The frequency results, which are shown in Fig. 24a, b, illustrate that the system maintains periodic-2 motion during acceleration and periodic-1 motion during deceleration.

In the region of 555–576 rad/s, both the bistable behaviour and hysteretic cycle appear. The frequency results show that the system maintains periodic-2 motion during acceleration and quasiperiodic motion during deceleration, as shown in Fig. 24c, d. This experiment can provide proof of the bistable behaviour and hysteretic cycle revealed in Sect. 2.2.

It should be noted that in Fig. 24c, there are more than 2 peaks. But it can be known from the orbit result, Fig. 25c, and phase space reconstruction result, Fig. 26c, the system maintains periodic-2 motion under this condition. The excess peaks should be caused by ambient interference.

In addition, this experiment also found that when the eccentric distance of the rotor decreases, both the first and second bistable region decrease, and the hysteretic cycle weakens gradually. When the eccentric distance is smaller than the critical value (for this rotor, the critical value is 2 g mm), the bistable behaviour and hysteretic cycle almost disappear, as shown in Fig. 23b–d.

6 Conclusion

This manuscript built a dynamic model of a rod-fastened rotor considering damping of the interface. The fourth-order Runge–Kutta method was applied to illustrate the effect of damping of the interface on the

nonlinear dynamic behaviour of the rod-fastened rotor. The following conclusions can be obtained from the above analysis.

1. Due to the nonlinear oil film force, the rod-fastened rotor-bearing system presents bistable behaviour and hysteretic cycle. The damping of the interface has a great influence on this characteristic.
2. In terms of the bifurcation behaviour, when the damping of the interface is ignored, there are two instability behaviours: periodic-2 motion and quasiperiodic and chaotic motion, where the periodic-2 motion corresponds to the peak of the transient response, and quasiperiodic and chaotic motion corresponds to the hysteresis cycle behaviour of the transient response. Once the damping of the interface is considered, the first two unstable speeds increase significantly, the first unstable interval increases, and the second unstable interval decreases. In addition, a third instability behaviour occurs, which includes periodic-2 and periodic-4 motion. Among them, the first unstable behaviour corresponds to the peak of the transient response, and the second unstable behaviour corresponds to the hysteresis cycle behaviour of the transient response.
3. In the aspect of transient response, when damping of the interface is ignored, there is no hysteretic cycle behaviour in the process of acceleration, and the hysteretic cycle in the process of deceleration is relatively gentle. When damping of the interface is considered, the hysteretic cycle occurs in both the acceleration and deceleration progress, and the vibration curve during hysteretic cycle is relatively steeper.
4. A rod-fastened rotor-bearing test bench is set up to verify the bistable behaviour and hysteretic cycle. In addition, it is found that the eccentric distance of the rotor has a great effect on the bistable behaviour. When the eccentric distance is small enough, the bistable behaviour and hysteretic cycle disappear.

Acknowledgements This work was supported by the National Science and Technology Major Projects (2017-IV-0010-0047) and National Natural Science Foundation of China (No. 51976214). References [22, 23] provided valuable ideas for the research of this paper. The first author acknowledges Associate Professor Yang Jun of University of Shanghai for Science and Technology and Master Ting-feng Yan of East China University of Science and Technology. The authors acknowledge all the doctors, nurses and volunteers who contributed to the fight against COVID-19.

Funding The authors have not disclosed any funding.

Data availability The data can be made available on reasonable request.

Declarations

Conflict of interest The authors declare that they have no conflict of interest.

References

1. Peng He: Research on the Influences of Elastic-Plastic Contact and Temperature Distribution on Tie-Bolted Fastened Rotor Dynamics. Harbin Institute of Technology, Harbin (2013) (**in Chinese**)
2. Ehrich, F.F.: Some observation of chaotic vibration phenomena in high-speed rotor-dynamics. J. Vibr. Acoust. **113**(1), 50–57 (1991)
3. Li, W., Yang, Y., Sheng, D., Chen, J.: A novel nonlinear model of rotor/bearing/seal system and numerical analysis. Mech. Mach. Theory **46**(5), 618–631 (2011)
4. Plantegenet, T., Arghir, M., Jolly, P.: Experimental analysis of the thermal unbalance effect of a flexible rotor supported by a flexure pivot tilting pad bearing. Mech. Syst. Signal. Pr. **145**, 1–16 (2020)
5. Akay, M.S., Shaw, A.D., Friswell, M.I.: Continuation analysis of a nonlinear rotor system. Nonlinear Dyn. **151**, 1–19 (2021)
6. Li, S., Xu, Q., Zhang, X.: Nonlinear dynamic behaviors of a rotor-labyrinth seal system. Nonlinear Dyn. **47**(4), 321–329 (2006)
7. Liang, H.U.: Research on the Nonlinear Dynamic Characteristics of Gas Turbine Circumferential Rod Fastening Rotor. North China Electric Power University, Beijing (2016).. (**in Chinese**)
8. Xia, K., Sun, Y., Hong, D., Guo, J., Kang, X.: Effects of contact interfaces on rotor dynamic characteristics of heavy-duty gas turbine generator set. In: IEEE International Conference on Mechatronics and Automation, pp. 714–719 (2016)
9. Li, Y.: Analysis of Bistable Characteristics of a Biased Disk Rotor with Squeeze Film Damper. Civil Aviation University of China, Tianjin (2019).. (**in Chinese**)
10. Hei, D., Lu, Y., Zhang, Y., Liu, F., Zhou, C., Müller, N.: Nonlinear dynamic behaviors of rod fastening rotor-hydrodynamic journal bearing system. Arch. Appl. Mech. **85**(7), 855–875 (2015)
11. Hei, D., Lu, Y., Zhang, Y., Lu, Z., Gupta, P., Müller, N.: Nonlinear dynamic behaviors of a rod fastening rotor supported by fixed–tilting pad journal bearings. Chaos Soliton Fractals **69**, 129–150 (2014)

12. Hei, D., Zheng, M.: Investigation on the dynamic behaviors of a rod fastening rotor based on an analytical solution of the oil film force of the supporting bearing. J. Low Freq. Noise Vibr. Act. Control **1**, 1–33 (2020)
13. Li, Y., Luo, Z., Liu, Z., Hou, X.: Nonlinear dynamic behaviors of a bolted joint rotor system supported by ball bearings. Arch. Appl. Mech. **89**(7), 3046–3061 (2019)
14. Sun, W., Yan, Z., Tan, T., Zhao, D., Luo, X.: Nonlinear characterization of the rotor-bearing system with the oil-film and unbalance forces considering the effect of the oil-film temperature. Nonlinear Dyn. **92**(3), 1119–1145 (2018)
15. Haslam, A.H., Schwingshackl, C.W., Rix, A.I.J.: A parametric study of an unbalanced Jeffcott rotor supported by a rolling-element bearing. Nonlinear Dyn. **219**(99), 1–34 (2020)
16. Alves, D.S., Machado, T.H., Cavalca, K.L., Bachschmid, N.: Characteristics of oil film nonlinearity in bearings and its effects in rotor balancing. J. Sound Vibr. **459**, 1–19 (2019)
17. Zhao, S.X., Dai, X.D., Meng, G., Zhu, J.: An experimental study of nonlinear oil-film forces of a journal bearing. J. Sound Vibr. **287**(4), 827–843 (2005)
18. Zhuo, M., Yang, L.H., Yu, L.: Contact stiffness calculation and effects on rotor dynamic of rod fastened rotor. In: Proceedings of the ASME International Mechanical Engineering Congress and Exposition, pp. 1–8 (2016)
19. Qian, Z.W., Cheng, L., Chen, W., Li, Y.H.: Analysis on bistable response of a disk-rod-fastening rotor. Hangkong Dongli Xuebao **26**(7), 1563–1568 (2011). (**in Chinese**)
20. Zhang, F., Feng, Y., Guo, B., Li, J.: Impact of connection stiffness on vibration characteristics of rotor in circumferential tie rod rotor of gas turbine. Tuijin Jishu **42**(5), 10–19 (2020). (**in Chinese**)
21. Li, C., Zhengwen, Q., Wei, C., Jiadong, F.: Influence of structural parameters on the bistable response of a disk-rod-fastening rotor. Zhendong Kongzhi Zhenduan **32**(5), 767–772 (2012). (**in Chinese**)
22. Wang, L., Wang, A., Jin, M., Yin, Y.: Study on bistable vibration characteristics for rod fastening rotor considering internal damping. Zhongguo Jixie Gongcheng **32**(5), 12–23 (2020). (**in Chinese**)
23. Wang, L., Wang, A., Jin, M., Yin, Y., Heng, X., Ma, P.: Nonlinear dynamic response and stability of a rod fastening rotor with internal damping effect. Arch. Appl. Mech. **10**, 1–17 (2021)
24. Li, P., Yuan, Q.: Determination of contact stiffness and damping of a tie-bolt rotor with interference fits using model updating with thin-layer elements. Shock. Vibr. **1**, 1–10 (2020)
25. Liu, Y., Liu, H., Wang, N.: Effects of typical machining errors on the nonlinear dynamic characteristics of the rod-fastened rotor bearing system. J. Vibr. Acoust. **139**, 407–417 (2017)
26. Rao, X.B., Chu, Y.D., Chang, Y.X., Zhang, J.G., Tian, Y.P.: Dynamics of a cracked rotor system with oil-film force in parameter space. Nonlinear Dyn. **88**(4), 2347–2357 (2017)
27. Abdou, K.M., Saber, E.: Effect of rotor misalignment on stability of journal bearings with finite width. Alex. Eng. J. **59**(5), 1–11 (2020)
28. Zhang, Y., Fang, B., Kong, L., Li, Y.: Effect of the ring misalignment on the service characteristics of ball bearing and rotor system. Mech. Mach. Theory **151**, 1–16 (2020)
29. Yu, H., Ran, Y., Zhang, G., Li, X., Li, B.: A time-varying comprehensive dynamic model for the rotor system with multiple bearing faults. J. Sound. Vibr. **488**, 1–21 (2020)
30. Harsha, S.P., Sandeep, K., Prakash, R.: Nonlinear dynamic response of a rotor bearing system due to surface waviness. Nonlinear. Dyn. **37**, 91–114 (2004)
31. Zhang, H., Lu, K., Zhang, W., Fu, C.: Investigation on dynamic behaviors of rotor system with looseness and nonlinear supporting. Mech. Syst. Signal. Pr. **166**, 1–18 (2021)
32. Zhang, H., Lu, K., Zhang, W., Fu, C.: Nonlinear dynamic analysis of a rub-impact rotor supported by oil film bearings. Arch. Appl. Mech. **83**(3), 413–430 (2013)
33. Hu, L., Liu, Y., Teng, W., Zhou, C.: Nonlinear coupled dynamics of a rod fastening rotor under rub-impact and initial permanent deflection. Energies **9**(12), 883–902 (2016)
34. Silva, A., Zarzo, A., González, J.M.M., Munoz-Guijosa, J.M.: Early fault detection of single-point rub in gas turbines with accelerometers on the casing based on Continuous Wavelet Transform. J. Sound. Vibr. **487**, 1–21 (2020)
35. Xiang, L., Zhagn, Y.: Analysis and diagnosis of rotor crack fault based on morphological characteristics of axis orbit. Zhendong Kongzhi Zhenduan **39**(4), 760–769 (2019). (**in Chinese**)
36. Yang, Y., Yang, Y., Cao, D., Chen, G., Jin, Y.: Response evaluation of imbalance-rub-pedestal looseness coupling fault on a geometrically nonlinear rotor system. Mech. Syst. Signal Pr. **118**, 423–442 (2019)
37. Xiang, L., Gao, X., Hu, A.: Nonlinear dynamics of an asymmetric rotor-bearing system with coupling faults of crack and rub-impact under oil-film forces. Nonlinear Dyn. **86**(2), 1057–1067 (2016)
38. Tang, Y., Lin, F., Zou, Q.: Dynamical behavior analysis of rubbing rotor system under asymmetric oil film force. Math. Probl. Eng. **1**, 1–16 (2019)
39. Behzad, M., Alvandi, M.: Unbalance-induced rub between rotor and compliant-segmented stator. J. Sound Vibr. **429**, 96–129 (2018)
40. Srivastava, A.K., Tiwari, M., Singh, A.: Identification of rotor-stator rub and dependence of dry whip boundary on rotor parameters. Mech. Syst. Signal Pr. **159**(4), 1–16 (2021)
41. Mehrjooee, O., Fathollahi Dehkordi, S., Habibnejad Korayem, M.: Dynamic modeling and extended bifurcation analysis of flexible-link manipulator. Mech. Based Des. Struct. **46**, 1–24 (2019)
42. Capone, G.: Analytical description of fluid-dynamic force field in cylindrical journal bearing. L'Energia Elettr. **3**(3), 105–110 (1991)
43. Korayem, M.H., Dehkordi, S.F., Mehrjooee, O.: Nonlinear analysis of open-chain flexible manipulator with time-dependent structure. Adv. Space Res. **69**, 1027–1049 (2022)
44. Aghajari, M., Fathollahi Dehkordi, S., Korayem, M.H.: Nonlinear dynamic analysis of the extended telescopic joints manipulator with flexible links. Arab. J. Sci. Eng. **46**, 7909–7928 (2021)
45. General Editorial Board of Aeroengine Design Manual: Aeroengine Design Manual Rotor Dynamics Section. Aviation Industry Press, Beijing (2000).. (**in Chinese**)

46. Li, J., Li, Y., Cui, L., Mo, G., Zhong, W., Feng, Y.: Nonlinear dynamic behavior of circumferential rod fastened rotor with initial thermal deflection. J. Vibr. Eng. Technol. **1**, 1–14 (2021)
47. Lizi, S.: Research on Uncertainty of Rotor System based on Polynomial Chaos Expansion. Nanjing University of Aeronautics and Astronautics, Nanjing (2018).. (**in Chinese**)
48. Zhushi Rao: A Study of Dynamic Characteristics and Contact Stiffness of the Rod Fastening Composite Special Rotor. Harbin Institute of Technology, Harbin (1982) (**in Chinese**)
49. Yuan, Q., Gao, R., Feng, Z., Wang, J.: Analysis of dynamic characteristics of gas turbine rotor considering contact effects and pre-tightening force. In: ASME Turbo Expo: Power for Land, Sea, Air, pp. 1–6 (2008)
50. Jiang, S., Zheng, Y., Zhu, H.: A contact stiffness model of machined plane joint based on fractal theory. J. Tribol.-T ASME **132**, 1–7 (2010)
51. Zhang, F.: Research on the Impact of Gas Turbine Tie Rod Rotor Connection Stiffness on Rotor Dynamics Characteristics. University of Chinese Academy of Sciences, Beijing (2020).. (**in Chinese**)

Publisher's Note Springer Nature remains neutral with regard to jurisdictional claims in published maps and institutional affiliations.